

# Shadow Imaging of Geosynchronous Satellites: Simulation, Image Reconstruction, and Shadow Prediction

Dennis M. Douglas<sup>1\*</sup>  
Bobby R. Hunt<sup>1</sup>  
David G. Sheppard<sup>1</sup>

<sup>1</sup>*Integrity Applications Incorporated, 535 Lipoa Parkway, Ste 101, Kihei, USA*

## Abstract

Shadow imaging is a technique to obtain highly resolved silhouettes of resident space objects (RSOs) which would otherwise be unattainable using conventional terrestrial based imaging approaches. This is done by post processing the measured irradiance pattern (shadow) cast onto the Earth as the RSO occults a star. The research presented here focuses on shadow imaging of geosynchronous (GEO) satellites with near stationary orbits approximately 36,000 km from the Earth. Shadows pertaining to a set of diverse observing scenarios are simulated and used as inputs to a Fresnel based phase retrieval algorithm. Spatial resolution limits are evaluated and correlated to signal to noise (SNR) metrics. Resolvable feature sizes of less than 1 m are shown to be readily achievable using foreseeable observing scenarios. The development of a shadow prediction capability is outlined with initial output indicating that there are, on average, over 1000 shadows on the Earth on any given time from a single GEO satellite for stars brighter than  $m_v=10$ . Shadow ground track uncertainties are correlated to stellar astrometric errors. Global and localized shadow track maps are presented demonstrating a high feasibility for future shadow collections.

## 1 INTRODUCTION

### 1.1 Motivation

GEO satellites are essential for modern communication networks, precision GPS access, weather forecasting, television broadcasts, and many defense/intelligence applications. Over the past half century more than 1000 GEO satellites have been launched and placed into orbit and the trends indicate that this population will continue to grow at an exponential rate. The world's reliance on GEO satellites cannot be overstated, and this dependence will continue to grow in multiple forms in the years to come. Due to the GEO orbital range, the largest terrestrial based optical telescopes are only capable of capturing imagery with resolvable features of several meters on GEO satellites. If a malfunction occurs upon orbit insertion such as a solar panel not deploying or an antenna getting snagged there is no direct way to observe it from Earth in finely resolved detail. Using conventional imaging techniques the attainable spatial resolution is limited by the Rayleigh criterion,

$$d_r = 1.22 \frac{\lambda}{D} z, \quad (1)$$

where the smallest resolvable spatial feature is  $d_r$ ,  $\lambda$  is the observation wavelength,  $D$  is the light collection aperture diameter, and the distance to the object of interest is denoted by  $z$ . Using  $\lambda = 400$  nm, an 18 m telescope is needed to resolve a 1 m feature on a GEO satellite, and a 35 m aperture is needed to resolve a 0.5 m feature.

### 1.2 Background

Shadow observations are made of distant RSOs from an Earth based observing system by measuring the irradiance distribution (shadow) on the ground resulting from an occultation event of the RSO passing in front of a star. In the context of a conventional lab based diffraction experiment the star that is occulted is the light source, the occulting

---

\*Send correspondence to Dennis M. Douglas: E-mail: ddouglas@integrity-apps.com

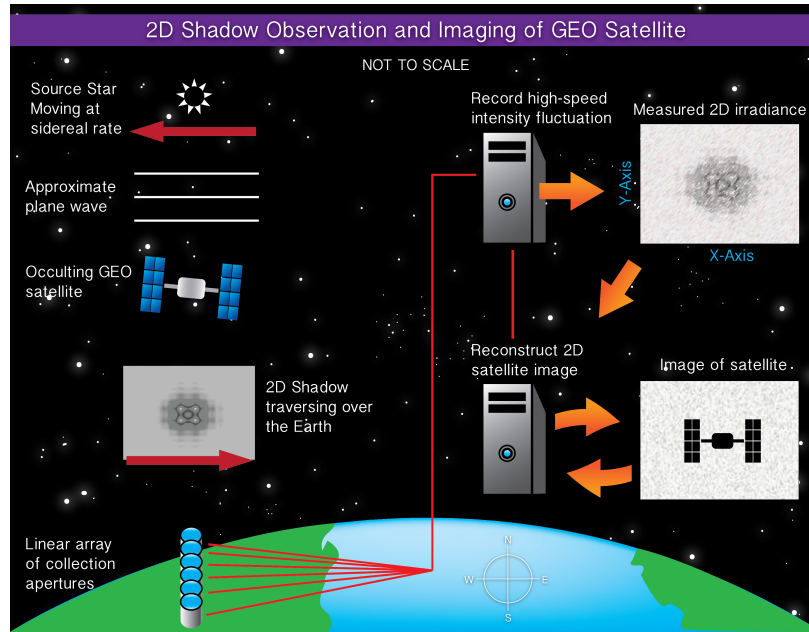


Figure 1: Two dimensional shadow observation (imaging) of geosynchronous satellite. An linear array of individual apertures on the Earth is used to collect light as the 2D shadow traverses over it. A 2D measurement of the irradiance pattern is obtained and iteratively reconstructed to yield an image of the occulting satellite. Note, the depiction is not to scale.

RSO is an obscuration at the "aperture plane", and the observer on the Earth's surface performs a measurement of the diffraction pattern at the "observation plane." Given the very large astronomical distances to stars the light incident on the occulting RSO is approximated as a continuous set of plane waves yielding a polychromatic incoherent source. For a star with an appreciable angular extent the light can be modeled as a radially distributed set of plane waves. Shadow observation using a single collection aperture was first proposed in 1952 by *Taylor*, and a shadow of the asteroid Pallas was first successfully observed in 1978.[1, 2] Earth based shadow observations remain the most accurate method to calculate an asteroid's size and shape other than measurements made from venturing spacecraft in the solar system. Techniques have been developed to study distant objects in the Kuiper Belt and Oort Cloud using serendipitous observations of stellar occultations.[3]

The idea of shadow imaging of GEO satellites using a linear array of small collection apertures coupled to high speed detectors was first proposed in 2005 by *Burns, et al.*[4] Here it was demonstrated that an iterative phase retrieval algorithm can be implemented to recover the satellite's 2D transmission function which is equivalent to a reverse contrast image. Shadow imaging of GEO satellites was examined in further detail in 2008 by *Luu, et al* introducing the concept of spectrally resolved shadow imaging which seeks to increase the amount of attainable spatial resolution while facilitating higher SNR.[5] This is achieved by splitting the collected light into spectral bins and performing the image reconstruction separately on each bin. The final image results from stacking the individual reconstructed images from each spectral bin. Work by *Douglas* in 2014 then examined the image resolution limits of shadow imaging using a radiometrically based wave optics simulation approach by varying environmental, observational, and light collection parameters.[6]

The representative size of GEO satellites combined with their orbital distance results in the ground shadow being consistent with diffraction phenomena associated with the Fresnel region when observing at visible wavelengths. Shadow imaging fundamentally differs from conventional imaging in that as the collection apertures get smaller the attainable resolution increases. Furthermore, all past efforts indicate that shadow imaging is very resilient to atmospheric turbulence. An illustration of the end to end shadow imaging process using a linear array of collection apertures is shown in Figure 1.

In Sec. 2 we present recent shadow simulation developments and outline the process to generate truth and measurement inferred shadows. A set of simulation cases, spanning diverse observational scenarios, are presented and vary in SNR. Sec. 3 details the image reconstruction process using a Fresnel integral propagation kernel. Final images

of the simulation cases are presented and correlated to SNR metrics. Advances in our shadow prediction capability are covered in Sec. 4 which include global density maps, localized shadow tracks, and track uncertainties associated with astrometric errors.

## 2 SHADOW SIMULATION

The shadow simulation is performed using a radiometrically based numerical waveoptics propagation which generates the truth shadows as described in Sec. 2.1. The light collection and measurement processes are then modeled in the simulation per Sec. 2.2 to yield the measurement inferred shadows. The measurement inferred shadows are then used in the reconstruction process detailed in Sec. 3.

### 2.1 Truth Shadow

Monochromatic irradiance patterns  $I(r; \lambda_i)$  are generated over a wavelength range  $\lambda_a \rightarrow \lambda_b$ . Each  $I(r; \lambda_i)$  results from a multi step waveoptics propagation from the satellite plane to the observation plane. The following sequential steps are used to create each  $I(r; \lambda_i)$ :

1. Generate exoatmospheric complex electric field  $U_S(r_o; \lambda_i)$  emerging from satellite plane based on source star's brightness  $m_v$  and angular extent  $\alpha$ , and satellite's transmission function.
2. Propagate  $U_S(r_o; \lambda_i)$  from satellite to top of atmosphere.
3. Generate altitude dependent random phase screens based on  $C_n^2$  profile and apply to electric field as it propagates through the atmosphere to the ground.
4. Convert electric field on ground to irradiance.
5. Multiply irradiance by atmospheric transmission factor.
6. Shift irradiance pattern based on refraction per look angle relative to zenith.

The monochromatic shadows  $I(r; \lambda_i)$  are then summed within each spectral bin  $\Lambda_j$  to produce a set of polychromatic shadows  $I(r; \Lambda_j)$  as shown by (2). The number of spectral bins  $J$  within the full wavelength range is  $\frac{\lambda_b - \lambda_a}{\mathbb{I}}$ , where  $\mathbb{I}$  is the width of each spectral bin. For example a full wavelength range of 400 to 900 nm using spectral bin widths of 10 nm, yields 50 spectral bins.

$$I(r; \Lambda_j) = \sum_{i=1}^{\mathbb{I}} I(r; \lambda_i) \quad (2)$$

The propagation through the vacuum and atmospheric regions are each performed using multiple steps by maintaining that  $\Delta < \frac{\lambda z}{L}$ , where  $\Delta$  is the grid spacing in the propagation plane,  $z$  is the propagation distance, and  $L$  is the support length extent. The propagation plane parameters were chosen to be  $\Delta = 0.1$  m,  $L = 100$  m, and  $M = 1000$ , where  $M$  is the number of grid points, to avoid sampling issues over a 400 to 900 nm wavelength range. The Hufnagel-Valley  $C_n^2$  profile with a coherence length of 5 cm and isoplanatic angle of 7  $\mu$ rad was used as the refractive index structure parameter to generate atmospheric phase screens.

### 2.2 Measurement Inferred Shadow

The measurement inferred shadows  $I_M(r; \Lambda_j)$  are generated using  $I(r; \Lambda_j)$ , along with the light collection system and detector parameters. Each aperture in the linear collection array has a diameter  $D$ . Thus the light collection process requires  $I(r; \Lambda_j)$  (size  $M \times M$ ) to downsize to  $M_{ap} \times M_{ap}$ , where  $M_{ap} = \frac{M}{D}$ , while maintaining radiometric accuracy. The following steps describe the simulation process for  $I(r; \Lambda_j) \Rightarrow I_M(r; \Lambda_j)$ :

1. Calculate the signal and sky background photon rate patterns based on  $D$ , the optical throughput, field of view, and sky background brightness.

2. The signal and background photon rates are then fed into a detector model which yields a stochastic realization of the measured polychromatic photon rate patterns which includes sensor noise.
3. The  $M_{ap} \times M_{ap}$  irradiance patterns are calculated then interpolated to the final  $M \times M$   $I_M(r; \Lambda_j)$  patterns.

The  $J$  measurement inferred irradiance patterns are then saved for use in the image reconstruction process. A set of 8 simulation cases were generated using the baseline parameters listed in Table 1. Case dependent input parameters are listed in Table 2, including spectral bin width, aperture size, and brightness and angular extent of the source star. The exposure time for each case is determined by how long it takes a point on the shadow to travel over a single aperture diameter length using a nominal shadow velocity of 2.6 km/s.

Table 1: Input parameters for generating the truth and measurement inferred shadows. Parameters that are varied per simulation case are indicated in red, all other parameters are common to each simulation case.

Propagation Parameters		Measurement Parameters	
Sampling	Value	Light Collection	Value
support length $L$	100 m	aperture size $D$	Per Case
grid spacing $\Delta$	0.1 m	field of view $\theta_a$	1 arcsec
grid samples $M$	1000	Spectral	Value
Object	Value	beginning $\lambda_a$	400 nm
Satellite Model	ResSat	ending $\lambda_b$	900 nm
Source Star	Value	width of $\Lambda_j$	Per Case
magnitude $m_v$	Per Case	number of bins $J$	Per Case
angular extent $\alpha$	Per Case	Detector	Value
Environmental	Value	exposure time $t$	Per Case
turbulence $C_n^2$	HV57	dark count rate $N_D$	200 Hz
sky brightness $m_B$	20 $m_v/\text{arcsec}^2$	detection efficiency $P_d$	0.5
Observational	Value	afterpulsing $P_{ap}$	0.1
off-zenith $\theta_v$	0 deg	gate time $t_g$	1 $\mu\text{s}$
latitude $\phi_{lat}$	0 deg	duty cycle $c_d$	0.95
longitude $\phi_{long}$	0 deg		
altitude $h$	0 m		

Truth and measurement inferred shadows were simulated in each spectral bin for each of the simulation cases. A resolution aperture composed of vertical and horizontal bars along with spoke patterns was used as the transmission function representing the satellite. The transmission function is shown in Figure 2 with notation indicating the size of the features. The simulated irradiance patterns  $I(r; \Lambda_1)$  and  $I_M(r; \Lambda_1)$  for the first spectral bin (400 to 500 nm) of Case 1B are shown in Figure 3.

Table 2: Varied input parameters for 8 simulation cases. Spectral bin width, aperture size, and brightness and angular extent of the source star are varied. All other simulation parameters are identical and listed in Table 1.

Case	Spectral Bin Width (nm)	Number of Spectral Bins	Aperture Size (m)	Star Brightness ( $m_v$ )	Star Extent ( $nrad$ )	Exposure Time (ms)
1A	10	50	0.4	8	0	15.3
1B	100	5	0.4	8	0	15.3
2A	10	50	0.4	11	0	15.3
2B	100	5	0.4	11	0	15.3
3A	10	50	0.4	8	20	15.3
3B	100	5	0.4	8	20	15.3
4A	10	50	0.8	11	0	30.6
4B	100	5	0.8	11	0	30.6

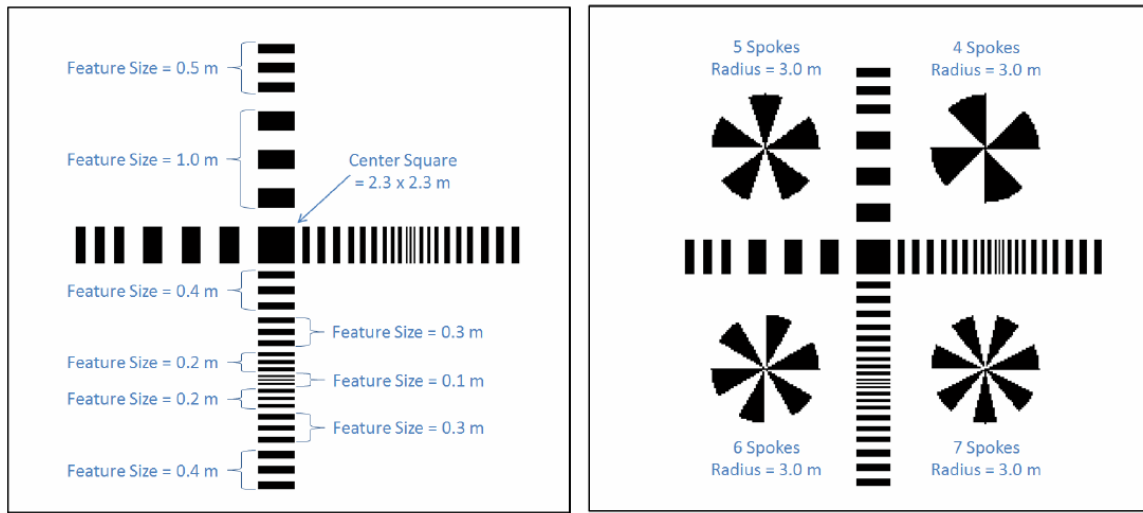


Figure 2: Resolution target composed of vertical and horizontal bars with widths and spacings varying from 1 m to 0.1 m, and patterns containing 5, 6, 7, and 8 spokes with a 3 m radius. This pattern was used as the transmission function of the satellite with the dark regions being completely opaque within an otherwise fully transmissive support plane. The images is zoomed in to illustrate small spatial features otherwise unseen in the full propagation plane support.

The SNR was calculated for each exposure time within each collection aperture using the geiger mode avalanche photo-diode (GM-APD) formalism developed by *Kolb*.<sup>[7]</sup> GM-APDs were chosen as the baseline detector technology due to their sensitivity to very low light levels and high speed detection capability. The center profile of the SNR using the first spectral bin for each of the simulation cases is shown in Figure 4.

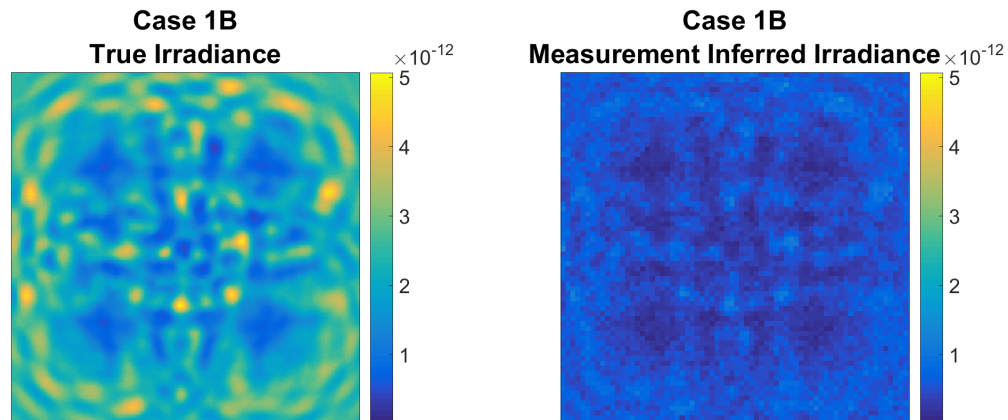


Figure 3: Irradiance pattern of first spectral bin for simulation Case 1B, with bin width of 100 nm. Left: True ground irradiance pattern. Right: Measurement inferred ground irradiance pattern. Displayed images represent only the center 28 x 28 m region of the full 100 x 100 m support plane to better illustrate the intensity fluctuations. Color bars are in units of  $W/m^2$ .

### 3 IMAGE RECONSTRUCTION

A Fresnel integral version of the iterative Gerchberg-Saxton [8] phase retrieval algorithm was used for image reconstruction on each simulation case. The steps performed in the image reconstruction process are as follows:

1. Generate an initial guess for the satellite's 2D transmission function,  $g_{q=0}(r_o)$ .
2. Forward Fresnel propagate  $g_{q=0}(r_o)$  from the satellite plane to the ground.
3. Replace the electric field amplitude at the ground with the amplitude derived from the intensity measurement  $I_M(r; \bar{\Lambda}_j)$  to yield  $u_{q=1}(r; \bar{\Lambda}_j)$ .
4. Back Fresnel propagate  $u_{q=1}(r; \bar{\Lambda}_j)$  from the ground to the satellite plane.
5. Replace the electric field phase at the satellite plane with the phase of the source star to yield  $u_{q+1}(r_o; \bar{\Lambda}_j)$ .

This represents a single iteration and is performed  $Q$  times to yield the reconstructed image  $u_Q(r_o; \bar{\Lambda}_j)$  for a single spectral bin. All the images for each spectral bin are then summed, and the result normalized, to form the final reconstructed image  $g'(r_o)$ .

All forward and back wave propagations are done using the average wavelength of each spectral bin. Thus, the forced ground amplitude is derived from  $I_M(r; \Lambda_j) \Rightarrow I_M(r; \bar{\Lambda}_j)$ , where  $\bar{\Lambda}_j$  is the average wavelength in the  $j^{th}$  spectral bin. The initial guess  $g_{q=0}(r_o)$  was set to be a uniform plane equal to the mean measured ground intensity, and each reconstruction uses  $Q = 10$  iterations. Using the Fresnel integral propagator instead of the Fraunhofer kernel allows the intensity ringing in the shadow patterns shown in Figure 3 to be exploited in the image reconstruction algorithm. Final image reconstructions for the simulation cases are shown in Figure 5. Resolution limits were determined for each case reconstruction, and listed in Table 3, based the known geometry of the resolution pattern in Figure 2 representing the satellite.

In cases with sufficient SNR, the resolution limits are shown to improve by a factor of 2X when the aperture size is halved. For the highest SNR cases 1A and 1B a 10X decrease in spectral bin width improves resolution by a factor of 2.5X. As the SNR is slightly decreased per cases 4A and 4B the same narrowing of spectral bin width improves resolution by 2X. For cases 2A and 2B the 10X narrower spectral bin width worsens the resolution by 0.6X due to

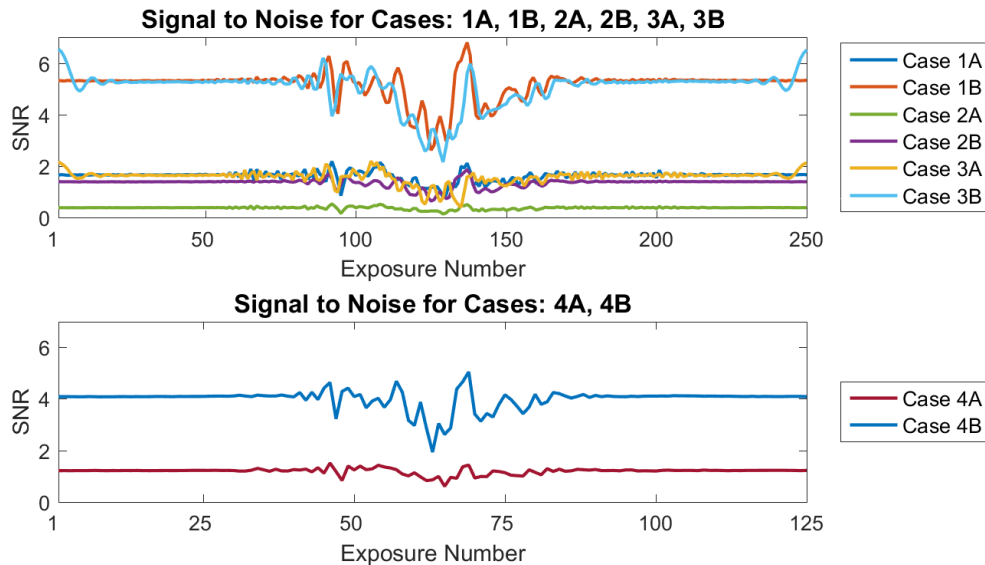


Figure 4: Signal to noise (SNR) ratio for center collection aperture for each simulation case. Top: Cases 1A, 1B, 2A, 2B, 3A, and 3B using 0.4 m diameter collection apertures resulting in 250 measurements over the shadow. Bottom: Cases 4A and 4B using 0.8 m diameter collection apertures yielding 125 samples of the shadow.

the very low SNR. Image quality is shown to be degraded as a function of support location (worsens radially outward from center) when using an extended source star without the non zero phase being implemented in the reconstruction algorithm at the satellite plane, as shown by cases 3A and 3B. However, these artifacts can be mitigated by applying the star's phase term during each iteration in the reconstruction algorithm.

Due to the diversity of potential observing scenarios the SNR can vary greatly if a single collection system configuration is used. For example, if small apertures are used in collection fine resolution can be obtained for bright source stars (high SNR), but resolution suffers for dim stars (low SNR). This also holds for the spectral bin width where bright stars favor narrower binning and dim stars warrant wider binning. Thus, for a given observational scenario, the combination of aperture size and spectral bin width should be optimized to obtain the best resolution. A dynamic collection system would be ideal such that it can be configured based on the observational scenario.

Table 3: Spatial resolution limits in final image reconstructions for simulation cases with baseline and varied input parameters quantified in Table 1 and Table 2. Resolvable feature sizes were determined based on known geometric bar and spoke patterns in the transmission function representing the satellite shown in Figure 2. Cases 3A and 3B were reconstructed with (Phase Comp.) and without (No Phase Comp.) applying the phase term at the satellite plane from the star's angular extent.

Case	Clear Resolvable Feature Size ( $m$ )	Threshold Resolvable Feature Size ( $m$ )
1A	$\geq 0.4$	0.3
1B	$\geq 1.0$	0.8
2A	$\geq 2.5$	2.3
2B	$\geq 1.5$	1.3
3A (No Phase Comp.)	Varied over Support	
3B (No Phase Comp.)	Varied over Support	
3A (Phase Comp.)	$\geq 0.4$	0.3
3B (Phase Comp.)	$\geq 1.0$	0.8
4A	$\geq 0.8$	0.7
4B	$\geq 1.6$	1.4



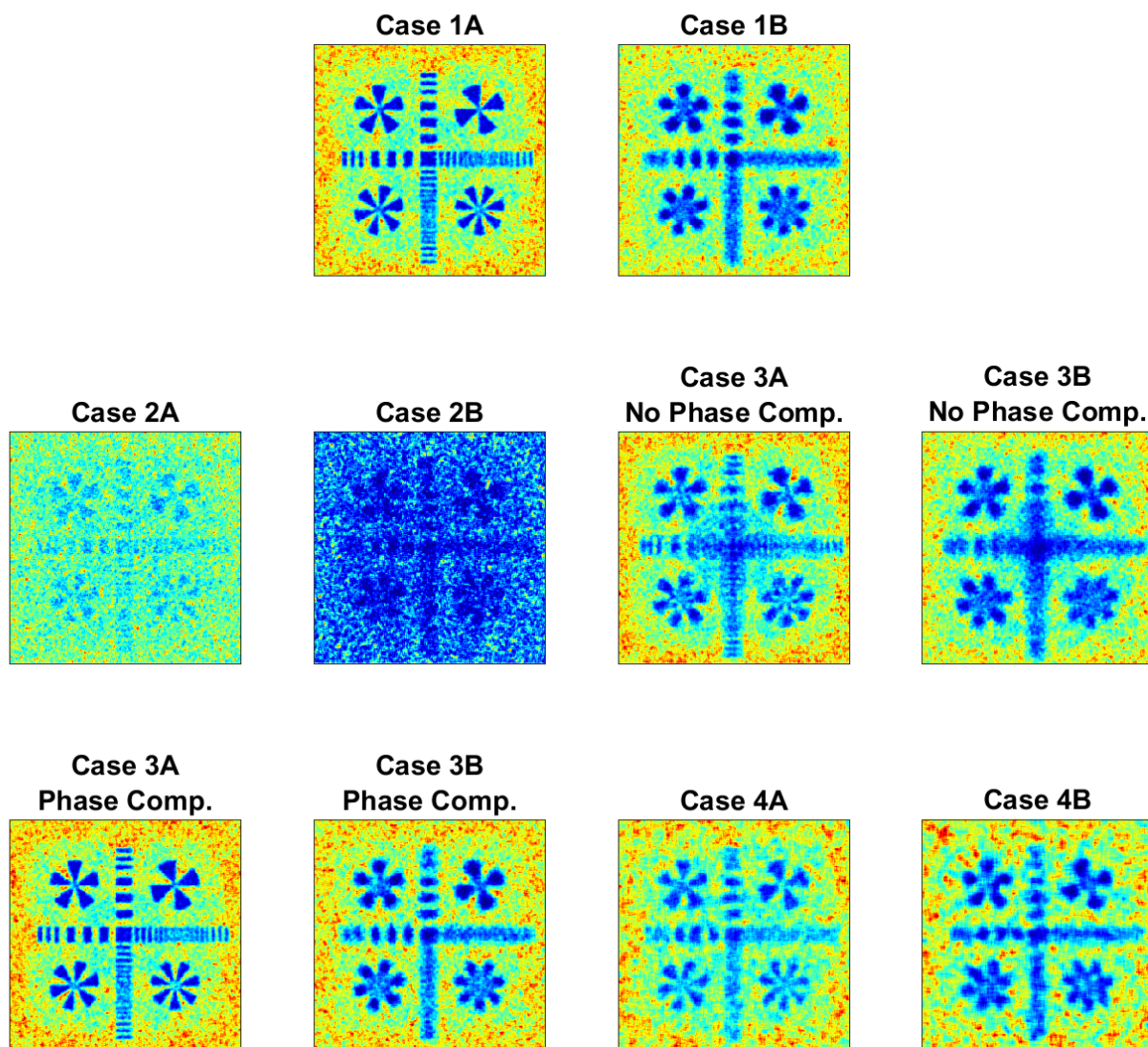


Figure 5: Final image reconstructions for simulation cases listed in Table 2 using a point source star. Higher resolution is exhibited when using narrower spectral bins (as seen in cases A versus B), and when using a smaller aperture size (as seen in cases 1 versus 2). Low SNR is also shown to decrease resolution as seen in the in cases 1 versus 2. Left: Angular extent of star was not taken into account with the star phase forced to be zero at satellite plane for each iteration in reconstruction algorithm. Right: Star extent taken into account with proper phase term being applied during each iteration in reconstruction algorithm. Displayed images represent only the center 28 x 28 m region of the full 100 x 100 m support plane to better illustrate resolution limits.



## 4 SHADOW PREDICTION

In shadow imaging it is of vital importance to deterministically calculate where to locate a terrestrial-based observation to ensure the shadow traverses over the collection system to effectively capture the occultation event. This is the problem of "being in the right place, at the right time." The methods used for predicting the shadow location on the earth from a stellar occultation are mainly geometric, although the earth atmosphere introduces complexity due to refraction. The purpose behind the prediction also influences the details of the implementation, particularly the scale and accuracy required. We have begun to study this problem and an outline of initial results and output capability from our developing shadow prediction tool are presented here along with an overview of the methodology.

### 4.1 Baseline Model

Given a point in time, or epoch, the positions of satellites of interest must be calculated. The starting point for this calculation is typically a Two Line Element (TLE) set. The TLE contains information which uniquely describes a satellite's orbit and position at a point in time. The TLE can be used to propagate the satellite along its orbit up to the epoch of interest and calculate its position in space. In this work, the satellite propagator SGP4 by *Vallado* is used.[9] These calculations are performed in an inertial frame known as TEME, and converted to Earth Centered Inertial (ECI).

With the ECI positions of the satellites in hand, it is necessary to compare these against a stellar astrometric catalog, also updated to the epoch of interest. Most catalogs list positions in terms of Julian Date 2000.0, or J2000.0. These positions must be updated to the current epoch by applying corrections for proper motion and radial velocity of each star. The updated catalog positions, which are also in the ECI frame, can be compared with the satellite positions. The particular frame of reference used in this work is known as the J2000.0/FK5 frame. There have been updates to the standard reference frames made by the international astronomical community during the past several years. The transition to these standards will be a subject of future work. The choice of star catalog is important since not all contain the same levels of positional accuracy. For this work, The Tycho-2 catalog provides positions for approximately 2.6 million stars. These positions have errors typically in the range 50-100 milli-arc-seconds (mas). The first data release from the Gaia mission is planned for September 2016, and will include an astrometric solution for all of the Tycho-2 stars as observed by Gaia. This data will have much better astrometric accuracy and will be used in future work. Additionally, the placement of the sensor system may be significantly influenced by the stars in the galactic plane where they are more dense. Figure 6 shows density plots of the where the galactic plane is clearly visible. Placing the sensor where the satellites are in front of the plane should enhance the probability of observing an occultation.

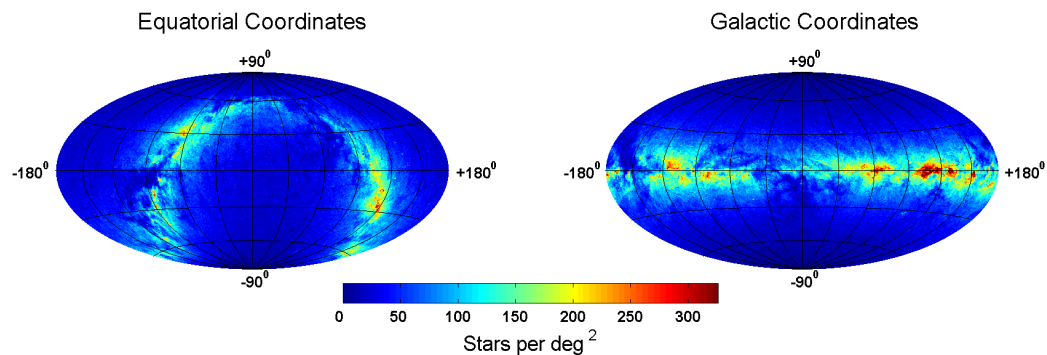


Figure 6: Density of stars per square degree in the equatorial coordinate system (left), and the galactic coordinate system (right). The spiral disk nature of the Milky Way galaxy is evident in the galactic coordinate representation. The equatorial coordinate representation illustrates the  $62.87^\circ$  inclination between the equatorial and galactic equators.

#### 4.1.1 Occultation Calculations

Given the above data, there are two paths forward to predicting the shadow locations. In the first case, a sensor is located at a particular site on the earth. Translating the site location to ECI provides a vector from the site to each satellite which identifies the sections of the celestial sphere which may contain an occulting star. Further processing is performed using this limited subset of the star to compute shadow tracks which should fall near the site. In the second case, no particular site is specified and the goal is to identify the location of all shadows cast on the earth by the satellites of interest. This is useful for computing shadow density maps useful in understanding which locations might be superior for placement of a sensor. For a particular shadow, the earth semi-radius as seen from the satellite provides angular bounds on the celestial sphere.

Given a star identified as a candidate for occultation, the next step is to compute where the ray from the star to the satellite intersects the earth. An algorithm by Pucinelli for locating the sensor boresight pointing is used in this work.[10] The earth is assumed to be a spheroid nominally sea level everywhere. The calculations may be localized for a site not at sea level by adjusting the polar and equatorial radii values appropriately. The algorithm poses the problem as the solution to a quadratic equation and provides both the near and far intersections. If there is no intersection, the result is imaginary. Only the near-side intersection is of interest, of course.

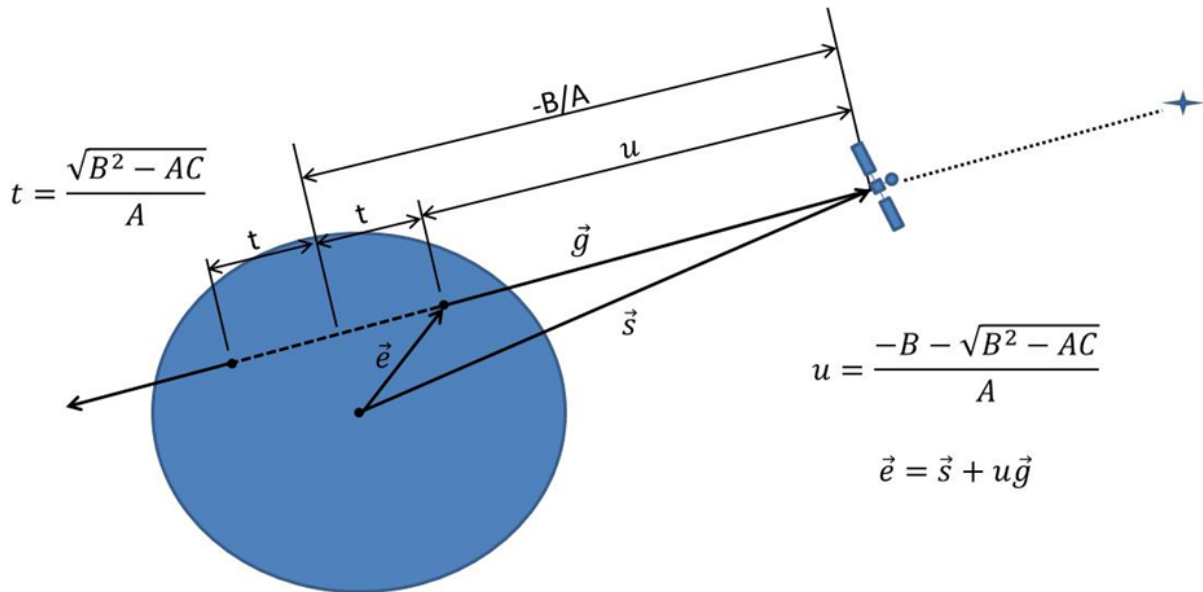


Figure 7: Earth intersection calculation from Pucinelli. Note: If  $u$  is complex then there is no intersection. Also, only the nearest intersection is of relevance.

#### 4.1.2 Refraction Calculations

Pucinelli provides a purely geometric solution. Refraction due to the earth atmosphere causes the shadow to be displaced from this idealized location. There are several approaches one could choose to address this problem. The highest fidelity approach might be to ray trace forward through many layers of the atmosphere. The index of refraction of air at each layer could be computed from a model of temperature and pressure as a function of height above the ellipsoid. Models such as the U.S. Standard Atmosphere or those provided in the Lowtran and Modtran products could be of use in this respect. Observations at low viewing elevations ( $\leq 20$  degrees) pose difficulties for the shadow imaging approach, as mentioned above. Above 20 degrees elevation, it is reasonable to pursue a one-step geometric solution for the shadow displacement, as described here. The one-step solution requires that we replace the troposphere/stratosphere model with what is known as the reduced atmosphere. This is also referred to as the homogeneous atmosphere. It refers to a single layer of air with the same density everywhere as at the surface, with vacuum above. It can be shown that this height is given by (3)

$$H = \frac{P}{g\rho} = \frac{RT}{g\mu} \quad (3)$$

where,  $g$  is the acceleration of gravity,  $\mu$  is the mean molecular weight of air,  $T$  is the temperature in Kelvins, and  $R$  is the gas constant with the appropriate units. A typical value for the height of the reduced atmosphere is 8 km. For the index of refraction of air in the reduced atmosphere, the following simplified solution shown in (4) serves well.

$$n_{TP} = 1 + 10^{-6} \left( 77.46 + \frac{0.459}{\lambda^2} \right) \frac{P}{T} \quad (4)$$

where  $\lambda$  is the wavelength in micrometers,  $P$  is the pressure in millibars, and  $T$  is the temperature in Kelvins. One of the advantages of this formulation is that the ratio  $\frac{P}{T}$  has convenient properties when interpreted as a random variable and can be used for Monte Carlo studies. The refraction at the upper boundary of the reduced atmosphere is given by (5).

$$r = \arcsin \left( \frac{nR \sin(z_0)}{R + H} \right) - \arcsin \left( \frac{R \sin(z_0)}{R + H} \right) \quad (5)$$

where  $n$  is the index of refraction of air,  $R$  is the radius of the earth,  $H$  is the height of the reduced atmosphere, and  $z_0$  is the zenith angle of the observation. This result is credited to the famous astronomer Giovanni Domenico Cassini, circa 1662. In recent studies, it has been shown to be very accurate above 20 degrees elevation. At 20 degrees elevation, the error is approximately 17 mas when compared to more computationally expensive algorithms based on numerical integration.[11] It is worth noting that the Cassini geometric solution is based on a spherical earth model. The calculation may be localized by using the effective radius of the earth to be the distance of the point on the ellipsoid from the center of the earth. The refraction angle and the corresponding displacement are very small, and so the approximation is reasonable.

To compute the shadow displacement, again assuming a spherical earth for simplicity, we utilize a result from Vallado regarding oblique sensor pointing field-of-view calculations. In this case, the sensor field-of-view is assumed to be the refraction angle  $r$ . Referring to Vallado, 4th Ed., Figure 11-10, the upper and lower boresight angles are given by (6) and (7).[9]

$$\eta = \arcsin \left( \frac{R \sin(z_0)}{R + H} \right) \quad (6)$$

$$\eta_{min} = \eta_{max} - r \quad (7)$$

where  $z_0$  is the zenith distance at the Pucinielli solution, and  $r$  is the refraction angle. Continuing on with the calculation, some intermediate results are computed in (8), (9), (10), and (11)

$$\gamma_{max} = \pi - \arcsin \left( \frac{(R + H) \sin(\eta_{max})}{R} \right) \quad (8)$$

$$\gamma_{min} = \pi - \arcsin \left( \frac{(R + H) \sin(\eta_{min})}{R} \right) \quad (9)$$

$$rho_{max} = R \cos(\gamma_{max}) + (R + H) \cos(\eta_{max}) \quad (10)$$

$$rho_{min} = R \cos(\gamma_{min}) + (R + H) \cos(\eta_{min}) \quad (11)$$

With these in hand, it is possible to compute the earth angles to the top and bottom of the refraction field of view as given by (12), (13), (14), and , (15).

$$\Lambda_{max} = \arcsin \left( \frac{\rho_{max} \sin(\eta_{max})}{R} \right) \quad (12)$$

$$\Lambda_{min} = \arcsin \left( \frac{\rho_{min} \sin(\eta_{min})}{R} \right) \quad (13)$$

$$\Lambda_{FOV} = \Lambda_{max} - \Lambda_{min} \quad (14)$$

$$b = R\Lambda_{FOV} \quad (15)$$

where  $R$  is the (effective) radius of the earth, and  $\Lambda_{FOV}$  is the total angle on the earth surface subtended by the oblique pointing.

## 4.2 Shadow Prediction Mapping

### 4.2.1 Global Shadow Density

We have developed the capability to map the density of shadows produced by one or more satellites. In Figure 8, one can see an example of this for the Galaxy 3C GEO satellite. The surface of the Earth is binned into 1 x 1 degree quadrangles to produce a histogram of shadows on the Earth surface for the night of Jan, 19th, 2016. The bin counts are normalized by the latitude dependent area of the quadrangle to produce a density map. The following constraints were added: 1) Latitude was confined to the range [-55,55]. 2) The viewing elevation angle was limited to be greater than 30 degrees. 3) Only stars with visual magnitudes of  $m_v=[2,10]$  were considered.

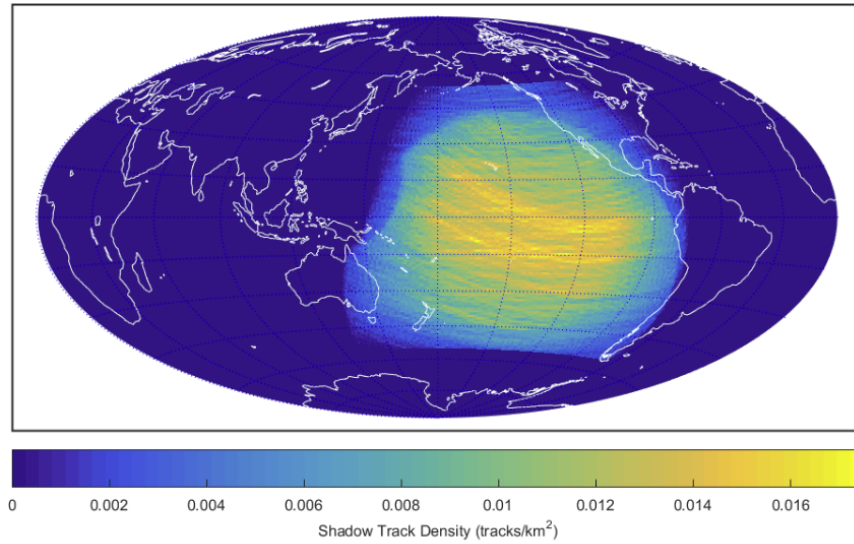


Figure 8: Shadow density map for GEO satellite Galaxy 3C on night of Jan. 19th, 2016. Latitude is confined to the range [-55,55]. The viewing elevation angle is limited to be greater than 30 degrees. Only stars with visual magnitudes of  $m_v=[2,10]$  were considered.

The temporal nature of shadow density maps has also been explored by creating one every ten days and making a movie of it. The significance of the changes is not clearly obvious to the eye, but may influence the optimization cost function in subtle ways. Corresponding to geographic shadow density, the rate at which the occultations occur during the same night, using the same constraints, is plotted in Figure 9 for different source star brightnesses. Here, it becomes apparent that there are a significant amount of shadows being cast onto the Earth from a single GEO satellite. Furthermore, the number of shadow events significantly increases as the stars get dimmer. The peak in shadow rate is attributed to the galactic plane aligning with the satellite relative to the Earth. This example suggests that at any given time during the night there are between 800 and 2000 shadows being cast onto the Earth from a single GEO satellite. Future work will include using multiple satellites and dimmer stars.

### 4.2.2 Localized Shadow Tracks and Uncertainties

Shadow trajectories over a localized region were also examined using our shadow prediction tool. The left of Figure 10 shows shadow tracks from GEO satellite YAMAL 300K (ID 38978) over a 2 x 2 km area near the technology park

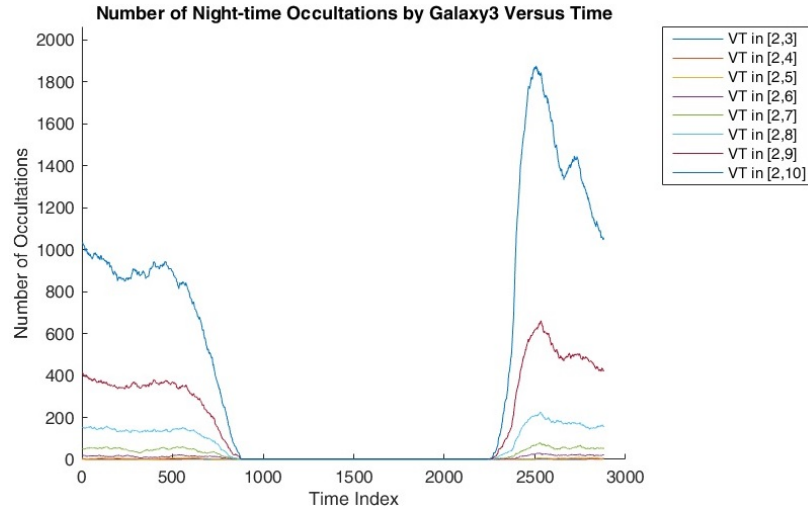


Figure 9: Number of occultations versus time for GEO satellite Galaxy 3C over a 24 hour period starting on Jan. 19th, 2016 using 0.5 s time steps. The middle portion corresponds to daytime for which shadow events are not calculated. Latitude is confined to the range  $[-55,55]$ . The viewing elevation angle is limited to be greater than 30 degrees. Only stars with visual magnitudes of  $m_v=[2,10]$  were considered.

in Kihei, HI on Maui for the night of Jan. 20th, 2016. The viewing elevation angle is limited to be greater than 30 degrees. Only stars with visual magnitudes of  $m_v=[2,10]$  were considered. For this particular night 25 shadow tracks traversed the 2 x 2 km region.

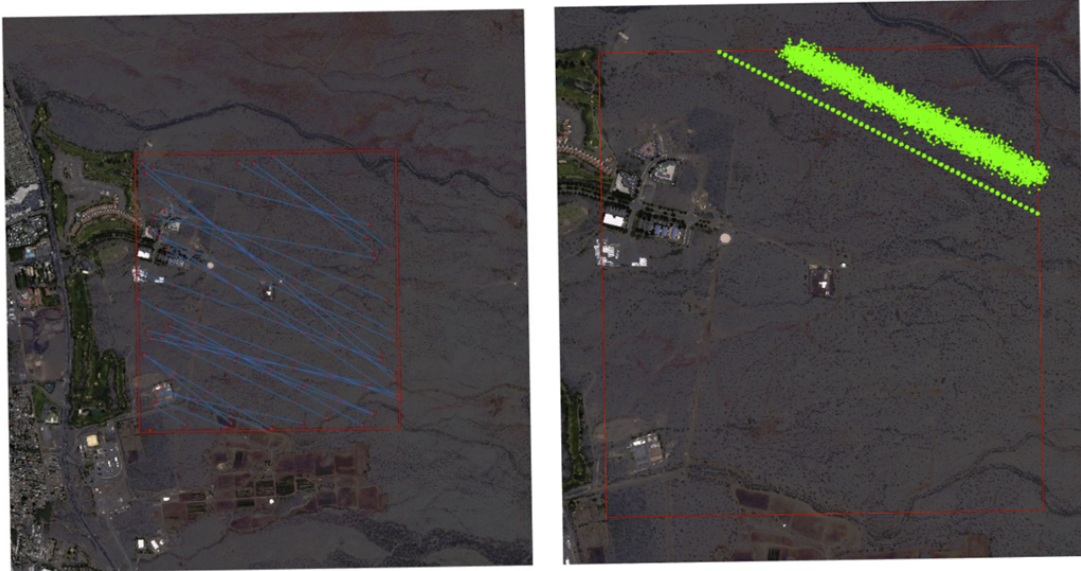


Figure 10: Left: Shadow tracks over 2 x 2 km area in Kihei, HI for the of night of Jan. 20th, 2016 from GEO satellite YAMAL 300K (ID 38978). Red dots are computed shadow locations at a 0.1 s time step. The blue lines are interpolated by the Matlab Mapping Toolbox plotm() function. Imagery is from the USGS Orthographic 1-foot database. The viewing elevation angle is limited to be greater than 30 degrees. Only stars with visual magnitudes of  $m_v=[2,10]$  were considered. Right: Monte Carlo of two shadow ground track uncertainties using 100 trials. Lower track uses a stellar position uncertainty of 9 mas, yielding a shadow track uncertainty of  $\sigma=2$  m. Upper track uses a stellar position uncertainty of 110 mas, yielding a shadow track uncertainty of  $\sigma=24$  m.



The impact of stellar astrometric errors on the shadow track location was also examined. Two near parallel shadow tracks were selected and different astrometric uncertainties were applied to each track. These two cases are shown in green highlight in the right of Figure 10, with an astrometric uncertainty in star position of 110 mas applied to the top track and an uncertainty of 9 mas to the bottom track. A Monte Carlo simulation using 100 trials was performed applying the astrometric errors per a Gaussian distribution resulting in the track uncertainties shown in the right of Figure 10. The larger 110 mas stellar uncertainty resulted in a ground track position with a standard deviation of  $\sigma=24$  m, while the smaller 9 mas star uncertainty yields  $\sigma=2$  m.

## 5 RESULTS AND FUTURE WORK

A robust end to end shadow simulation capability has been developed which generates monochromatic and spectrally binned irradiance patterns. A Fresnel integral version of the Gerchberg-Saxton phase retrieval algorithm was outlined and used for image reconstruction of simulated shadows over a diverse set of observational cases. Sub-meter image resolution is shown to be readily achievable in foreseeable shadow collection attempts. Aperture size and spectral binning width can be set based on a particular observation scenario to optimize resolution limits, suggesting a configurable collection system be considered. Image degradation from an extended source star is shown to be mitigated by applying the star's phase term during each iteration in the reconstruction algorithm. Future work will include implementing different collection geometries and detector technologies (CCD, CMOS, etc) in the shadow simulation, in addition to applying thresholding criteria in the image reconstruction process.

Initial results from our shadow prediction tool begins to characterize the solution space for the solving the optimization problem of collection system placement and for understanding the intricacies of predicting and capturing individual occultation events. Shadow density maps and localized shadow track predictions indicate that a significant number of shadow events from GEO satellites occur on a regular basis. Uncertainties in stellar astrometrics have been characterized per shadow ground track displacements using low and upward error bounds from the Tycho-2 star catalog. Future shadow prediction work will seek to identify optimal locations for collection system placement and range of mobility. In addition, we will begin to examine density of shadow events as a function of time throughout the year using multiple GEO satellites.

## ACKNOWLEDGMENTS

This work was supported by the United States Air Force Office of Scientific Research (AFOSR) grant FA9550-15-C-0035 and managed by Dr. Stacie Williams. We would like to thank Jeremy P. Bos and Michael C. Roggemann for discussions and insight regarding modeling atmospheric turbulence.

## References

- [1] Taylor, G. E., "An occultation by a minor planet," *Astronomical Society of South Africa* **11** (1952).
- [2] Wasserman, L., Millis, R. L., Franz, O. G., Howell, E., and White, N. M., "An occultation by a minor planet," *Astronomical Journal* **84** (1979).
- [3] Roques, F., Georgevits, G., and Doressoundiram, A., [*In the Solar System Beyond Neptune*], ch. The Kuiper Belt Explored by Serendipitous Stellar Occultations, University of Arizona Press (2008).
- [4] Burns, R. H., Gamiz, V., Dolne, J. J., Lambert, J., and Long, S., "Shadow imaging of geo satellites," in [*Proc. SPIE Unconventional Imaging*], (2005).
- [5] Luu, J., Jiang, L., and Willard, B., "Shadow imaging efforts at MIT Lincoln Laboratory," in [*Proc. Advanced Maui Optical and Space Surveillance Technologies Conference*], (2008).
- [6] Douglas, D., *Shadow Imaging of Geosynchronous Satellites*, PhD thesis, University of Arizona, Tucson (2014).
- [7] Kolb, K., "Signal-to-noise ratio of geiger-mode avalanche photodiode single-photon counting detectors," *Optical Engineering* **53**(8) (2014).



- [8] Gerchberg, R. W. and Saxto, W. O., "A practical algorithm for the determination of phase from image and diffraction plane pictures", *Optik* **35** (1972).
- [9] Vallado, D. A. and McClain, W. D., [*Fundamentals of Astrodynamics and Applications*], Springer (2001).
- [10] Puccinelli, E. F., "Ground location of satellite scanner data," *Photogrammetric Engineering and Remote Sensing* **42** (1976).
- [11] Young, A. T., "Sunset science. iv. low altitude refraction," *Astronomical Journal* **127** (2004).